Facile synthesis of monoclinic ammonium vanadate nanoflower and their applications for Aqueous ammonium-ion battery

Junjun Wang
Hunan University of Technology
Kaixiong Xiang
xiangkaixiong@sohu.com

Hunan University of Technology
Xiaoyu Wen
Hunan University of Technology
Han Chen
Hunan University of Technology
Jingxiong Liu
Hunan University of Technology

Research Article

Keywords: Aqueous ammonium-ions batteries, ammonium vanadate, nanoflower, Electrochemical performance

Posted Date: February 13th, 2024

DOI: https://doi.org/10.21203/rs.3.rs-3919481/v1

Additional Declarations: No competing interests reported.

Abstract

Ammonium ions (NH^{4+}) have gained significant attention in the field of energy storage due to their environmentally friendly nature, abundant resources, and fast diffusion. To improve the electrochemical performance of ammonium vanadate, we implemented a planar spacing approach, resulting in a highly efficient positive electrode material for aqueous ammonium ion batteries. Through our investigations, we successfully synthesized $NH_4V_4O_{10}$ with well-controlled planar spacing. This material demonstrated impressive electrochemical properties, including a discharge specific capacity of 297 mAh g^{-1} at 0.5 A g^{-1}, excellent rate performance with a capacity of 97 mAh g^{-1} at high current density (10 A g^{-1}), and a large ammonium ion diffusion coefficient ranging from 2.09×10^{-6} to 3.66×10^{-5} cm^2 S^{-1}. To further enhance its practical application, we combined $NH_4V_4O_{10}$ with polyaniline to assemble an aqueous ammonium ion full cell, achieving a high specific capacity of 88 mAh g^{-1} at 0.5 A g^{-1} and a remarkable energy density of 88 Wh kg^{-1} (at a power density of 500 W kg^{-1}). In-situ electrochemical tests revealed that $NH_4V_4O_{10}$ undergoes a phase transition to $(NH_4)_{1.92}V_3O_8$ during the first discharge process, and reversible hydrogen bond formation/breaking occurs during the ammoniation/deamination process. Moreover, our study successfully synthesized planar-spaced ammonium vanadate and highlights its exceptional electrochemical performance as a positive electrode material for aqueous ammonium ion batteries. The mechanistic insights gained from this study contribute to a deeper understanding of the behavior of ammonium vanadate within various structural frameworks.

1. Introduction

Rechargeable aqueous batteries exhibit significant advantages, such as high levels of safety, rapid ion conductivity, affordability, and environmental sustainability. These characteristics make them highly promising for extensive utilization in large-scale energy storage. Since the pioneering work of Dahn in 1994, who designed the first water-based lithium-ion battery, extensive research has been conducted on various metal ions, including K^+ [1], Na^+ [2], Zn^{2+} [3], Mg^{2+} [4], Ca^{2+} [5], and Al^{3+} [6], as charge carriers. In recent years, aqueous non-metal ion batteries, including NH^{4+} [7], H^+ [8], H_3O^+ [9], have gained increasing attention. Among the numerous non-metal cations, the ammonium ion (NH^{4+}) as a charge carrier exhibits more prominent attractiveness in terms of ultra-fast ion diffusion kinetics in low corrosive and low hydrogen evolution water electrolytes, as well as safety, resource abundance, and low-cost sustainable development advantages.

In 2012, Cui and colleagues [10] were the first to report on the utilization of the Prussian blue analogue $KM[Fe(CN)_6]$ (M = Cu,Ni) as an anode material for aqueous ammonium ion batteries. Following this, Ji et al. [7] reported the first "rocking chair" ammonium ion full cell, which used the Prussian white ammonium analogue $(NH_4)_{1.47}Ni[Fe(CN)_6]_{0.88}$ as the anode and 3,4,9,10 perylene tetracarboxylic diimide (PTCDI) as the negative electrode. Additionally, Ji's team investigated the hydrogen bonding chemistry between NH^{4+} and V_2O_5 [11], proposing a monkey swing model to illustrate its rich bonding chemistry with the electrode

body. Vanadium-based oxides with developed structures can efficiently store NH^{4+} due to their abundant redox reactions and large interlayer spacing. In previous works, two vanadium-based oxides/composites with varying morphologies and phase structures were synthesized for use as aqueous ammonium ion battery cathodes.

Both electrodes exhibited efficient ammonium storage performance. However, significant capacity degradation was observed at low current cycling in both electrodes, and most vanadium-based oxide cathodes suffered from vanadium dissolution problems. These studies suggest that using ammonium vanadate as the anode for aqueous ammonium ion batteries may be a promising option for achieving better electrochemical performance due to its unique advantages[12, 13].

Firstly, the NH^{4+} ions in the intercalated layer act as pillars between the V-O layers, preventing ion embedding delamination processes from destroying the structure while maintaining structural stability[14, 15]. Secondly, a N-H•••O hydrogen bonding network between the N-H groups and V-O layers increases structural stability, playing a pivotal role in improving the cycling stability of electrode materials[16, 17]. Lastly, compared to metal vanadates (e.g., Zn, K, Na, Ag, Cu), ammonium vanadates have smaller densities and relative molecular masses, resulting in higher bulk storage capacities. These advantages make ammonium vanadates potentially qualified cathode materials for aqueous ammonium ion batteries.

It is widely acknowledged that the reversible ion storage capacity of an electrode depends on its intrinsic properties, including planar spacing and structural characteristics. In this study, we devised a planar spacing strategy for ammonium vanadate to optimize its electrochemical performance as an anode in aqueous ammonium ion batteries. Two types of ammonium vanadates - V_3O_8-type $(NH4)_2V_3O_8$ and V_2O_5-type $NH_4V_4O_{10}$ - were synthesized via a one-step hydrothermal process and compared with V_3O_8-type $(NH_4)_2V_6O_{16}$. While all three materials exhibited reversible ammonium storage, they demonstrated distinct properties. The stable layered structure of the optimized ammonium vanadate suppresses cathode material dissolution, while sufficient ion transport channels facilitate fast ammonium ion reaction kinetics, resulting in excellent electrochemical performance for $NH_4V_4O_{10}$. For instance, it boasts a discharge specific capacity of 297 mAh g^{-1} at 0.5 A g^{-1}, high-rate capability (97 mAh g^{-1}@10 A g^{-1}), and a substantial ammonium ion diffusion coefficient (2.09×10^{-6}~3.66×10^{-6} cm^2 S^{-1}). Electrochemical results suggest that NH_4^+ possesses embedded pseudocapacitance features. Furthermore, through several non-in situ measurements, we confirmed that during the first discharge cycle of $NH_4V_4O_{10}$, it undergoes a partial phase transition to form $(NH_4)_{1.92}V_3O_8$ while exhibiting reversible hydrogen bond formation/breakage during the ammonification/deamination process. Overall, this study provides a detailed investigation into the electrochemical behavior of ammonium vanadate and enlightens us regarding the relationship among various structural frameworks.

2. Experimental Sectiion

2.1 Synthesis of $(NH_4)_2V_3O_8$

1.56 g of NH_4VO_3 and 1.44 g of $VOSO_4$ were solubilized in H_2O under magnetic agitation, followed by additional stirring for 30 min to generate a light-hued solution. The pH level was then manipulated to 10 with ammonia before being transferred into a 100 mL autoclave for hydrothermal heating at 80°C over the course of two hours. After filtration, the resulting solid products were subjected to oven drying at 60°C for six hours.

2.2 synthesis of $NH_4V_4O_{10}$

At a temperature of 80 ℃, NH_4VO_3 (1.1699 g) was dissolved in aqueous solution and agitated for a period of 15 minutes, following which oxalic acid (1.8912 g) was introduced and solubilized with the aid of a magnetic stirrer to yield a verdant solution. This resulting solution was subsequently transferred to a 100 mL autoclave and subjected to thermal treatment at an elevated temperature of 140 ℃ for 48 hours. Upon cooling, the solid end-product was harvested via filtration and then desiccated within an oven set at 110 ℃ for a duration of 6 hours.

2.3 synthesis of $(NH_4)_2V_6O_{16}$

Dissolve 1.5g of NH_4VO_3 in water under magnetic agitation to form a light yellow solution, and add hydrochloric acid to adjust the pH to 1.5 to produce an orange solution. Transfer the above solution to a 100 mL high-pressure hydrothermal kettle and heat the water at 180℃ for 36 hours. Filter and collect the solid product, which is then dried in an oven at 60℃ for 6 hours.

3. Materials characterization

The X-ray diffraction (XRD) patterns of the prepared sample were recorded by Ultima IV X-ray Diffractometer from Rigaku Corporation. Scanning electron microscopic images (SEM) were taken via a JEM-6700 F Scanning Electron Microscope. The X-ray photoelectron spectroscopy (XPS) was measured on Kratos Axis ULTRA tester from Perkin- Elmer. Fourier transform infrared spectroscopy (FT-IR) spectra were obtained by Thermofisher.

3.1 Electrochemical measurements

The prepared sample is used as the active material, and the slurry prepared from the active material, acetylene black, and poly(vinyl-idenefluoride) (PVDF) with a mass ratio of 8:1:1 is coated on the stainless-steel foil. Similarly, the counter electrode was prepared by coating the slurry with the mass ratio of activated carbon, acetylene black and polyvinyl fluoride (PVDF) at 8:1:1 on the stainless-steel foil. After drying and slicing, the electrode and the activated carbon anode are assembled into a CR2025 button cell. Use CHI660E and Neware CT-4008T for electrochemical testing (Based on the active substance mass of the cathode).

4. Results and discussion

Figure 1a illustrates the X-ray diffraction (XRD) pattern of the synthesized ammonium vanadate, where all the diffraction peaks of $(NH_4)_2V_3O_8$ correspond to $(NH_4)_2V_3O_8$ (PDF#51-1733), exhibiting lattice parameters of a = 8.899 Å, b = 8.899 Å, c = 5.5773 Å, α = γ = β = 90.0°. Similarly, all the diffraction peaks of $NH_4V_4O_{10}$ correspond to $NH_4V_4O_{10}$ (PDF#31–0075), possessing lattice parameters of a = 11.71 Å, b = 3.66 Å, c = 9.72 Å, α = γ = 90.0° and β = 101.0°. Furthermore, X-ray photoelectron spectroscopy (XPS) analysis in Fig. 1b confirms the high purity of prepared $NH_4V_4O_{10}$ consisting solely of V, O and N elements. The V 2p spectrum demonstrates four distinguishable peaks corresponding to V^{5+} (~ 517.7 and 525.0 eV for $2p_{1/2}$ and $2p_{3/2}$ respectively) and V^{4+} in $NH_4V_4O_{10}$ (~ 516.1 and 523.8 eV for $2p_{1/2}$ and $2p_{3/2}$ respectively), revealing a mixed oxidation state of V in the material. The N 1s spectrum depicts two distinctive peaks at 399.7 eV and 401.5 eV attributed to -N-H-(NH_3) and -N + H-(NH_4^+) moieties of ammonium ion respectively while the peak at 530.3 eV in O 1s spectrum indicates the existence of -VO- bond in $NH_4V_4O_{10}$ compound.

The scanning electron microscopy (SEM) images in Fig. 1 (c-e) have revealed distinct morphologies of the synthesized materials. Specifically, $(NH_4)_2V_6O_{16}$ exhibits a complete spatial structure characterized by layers composed of a nanoplate-like morphology. In contrast, $(NH_4)_2V_3O_8$ displays a uniform cube-shaped morphology, while $NH_4V_4O_{10}$ showcases a distinctive nanoflower-like structure. These diverse morphological configurations significantly influence their electrochemical characteristics. When utilized as cathode materials in ammonium-ion batteries, the three materials exhibit varying electrochemical performances due to their dissimilar structural arrangements. This is primarily attributed to the long diffusion path for ammonium ions and electrons during the ammonium-ion insertion/extraction process. Notably, the unique morphology of $NH_4V_4O_{10}$ demonstrates superior electrochemical properties compared to the other two materials.

The synthesized ammonium vanadates, namely $(NH_4)_2V_3O_8$, $(NH_4)_2V_6O_{16}$, and $NH_4V_4O_{10}$, exhibit interplanar distances of 5.6 Å, 7.9 Å, and 9.8 Å on their respective (001) faces as revealed in Fig. 2. As ion diffusion pathways and lattice dimensions play a pivotal role in electrochemical performance[18], $NH_4V_4O_{10}$ manifests the most expansive diffusive channels and outperforms the others in terms of high capacity, superior multiplicity performance, and prolonged cycling stability. Figure 2 showcases the crystal structures of these three ammonium vanadates with varying amounts of NH_4^+ ions occupying the central layer leading to diverse structural configurations. The monoclinic $NH_4V_4O_{10}$ is constituted by twisted VO_6 octahedra with vanadium units linked via edges to form a stable bilayer structure along the a-axis that comprises V_4O_{10} units stacked atop each other[19]. Notably, NH_4^+ ions act as "pillar" cations that stabilize the structure and mitigate volume variations during insertion or detachment of guest ions within interlayer gaps or channels[20]. The arrangement of $(NH_4)_2V_6O_{16}$ crystals is composed of VO_5 square cone units and twisted VO_6 octahedra, which collectively form a convoluted zigzag layer structure that aligns with the (00l) plane[21]. Meanwhile, $(NH_4)_2V_3O_8$ exhibits a layered and tunneled architecture

consisting of VO_5 square pyramids with shared vertices and VO_4 tetrahedra. Such structures that possess laminar or tunneling features are capable of furnishing two-dimensional interstitial spaces for NH_4^+ intercalation, mitigating mechanical stresses arising from volumetric changes, as well as shortening diffusion distances[22, 23]. From an atomic configuration perspective, all singly-bonded oxygen atoms present in the $NH_4V_4O_{10}$ and $(NH_4)_2V_3O_8$ layers can strongly interact with NH_4^+, whereby the stable and firmly anchored NH_4^+ ions function as robust "pillars" that consolidate the framework. Conversely, $(NH_4)_2V_6O_{16}$ comprises both single- and triple-bonded oxygen atoms on its surface layer. The triple-bonded oxygen atoms are unable to foster strong interactions with NH_4^+, leading to structural instability[24].

In order to further investigate the electrochemical behavior of the synthesized ammonium vanadates, $NH_4V_4O_{10}$, $(NH_4)_2V_3O_8$, and $(NH_4)_2V_6O_{16}$, a 2025-type button cell was assembled utilizing 0.5 mol L^{-1} $(NH_4)_2SO_4$ as the electrolyte. The cyclic performance of ammonium vanadate at a current density of 0.5 A g^{-1} within a voltage range of -1.5 to 1.5 V is depicted in Fig. 3. Notably, $NH_4V_4O_{10}$ exhibits an impressive initial discharge capacity of 297 mAh g^{-1}, which gradually declines over time but still retains a discharge capacity of 188 mAh g^{-1} after undergoing 100 cycles, surpassing that of $(NH_4)_2V_3O_8$ and $(NH_4)_2V_6O_{16}$. In contrast, $(NH_4)_2V_3O_8$ initially demonstrates a specific discharge capacity as high as 191 mAh g^{-1}; however, its capacity decays due to structural collapse. Moreover, while the $(NH_4)_2V_6O_{16}$ electrode showcases excellent cycling stability, it has a lower specific capacity at only 73 mAh g^{-1}. The underlying reasons for $NH_4V_4O_{10}$'s decline in capacity compared to those of $(NH_4)_2V_6O_{16}$ and $(NH_4)_2V_3O_8$ will be elaborated upon later on.

The electrochemical performance of $(NH_4)_2V_6O_{16}$, $(NH_4)_2V_3O_8$, and $(NH_4)_2V_6O_{16}$ as positive electrodes, with polyaniline (CC@PANI) electrodeposited on carbon cloth as the negative electrode and 0.5 mol L^{-1} $(NH_4)_2SO_4$ as the electrolyte, was evaluated in a buckle cell at a voltage window of 0.001 ~ 1 V and a current density of 0.5 A g^{-1}, as depicted in Fig. 3b. $NH_4V_4O_{10}$ demonstrated an exceptional initial discharge capacity of 88 mAh g^{-1} and an impressive energy density of 88 Wh kg^{-1} (power density of 500 W kg^{-1}), followed by gradual capacity reduction; nevertheless, it still exhibited a discharge capacity of 54 mAh g^{-1} after undergoing 100 cycles, surpassing those of both $(NH_4)_2V_3O_8$ and $(NH_4)_2V_6O_{16}$. Despite exhibiting slight capacity decay, $NH_4V_4O_{10}$ still displayed remarkable electrochemical performance.

$NH_4V_4O_{10}$ demonstrated specific capacities of 387, 304, 205, 163, 143, and 97 mAh g^{-1} at current densities of 0.2, 0.5, 1, 5, 8, and 10 A g^{-1} respectively. In contrast, $(NH_4)_2V_3O_8$ exhibited inferior specific capacities of only 187, 147,114,81 ,70, and 62mAh g^{-1} at the corresponding current densities whereas $(NH_4)_2V_6O_{16}$ recorded a meager capacity of just 46,44 ,36 ,32 ,30, and28mAh g^{-1} under similar conditions. When the current density was lowered to an intensity of 0.2 Ag^{-1}, the capacity reverted to its initial value thus attesting to its stable crystal structure and high electrochemical reversibility. The

superior capacity and multiplicative performance demonstrated by $NH_4V_4O_{10}$ when compared with $(NH_4)_2V_3O_8$ and $(NH_4)_2V_6O_{16}$ can be attributed to its large interlayer spacing, rapid ammonium ion diffusion, and copious abundance of easily adjustable active sites[25]. When $NH_4V_4O_{10}$ underwent discharge under low current densities of 0.2 and 0.5 A g^{-1}, it exhibited a propensity towards specific capacity decay; however, this trend was not observed at higher rates, which corresponded to its cycling performance (Fig. 3c). This occurrence can be attributed to the sluggish insertion mechanism at low currents that results in an elevated discharge capacity during the initial stage[26–28]. Nevertheless, successive cycles lead to volume expansion and structural degradation, leading to a gradual decline in capacity. Previous literature suggests that ions tend to rapidly accumulate at the electrode interface during high current densities. Hence, repeated NH_4^+ insertion/detachment-induced structural degradation can be significantly mitigated under high current conditions.

The initial charge-discharge profiles of $(NH_4)_2V_6O_{16}$, $(NH_4)_2V_3O_8$, and $NH_4V_4O_{10}$ electrodes under current densities ranging from 0.2 to 8 A g^{-1} are illustrated in Figs. 3d ~ 3f. It is noteworthy that the discharge-charge curves of ammonium vanadate exhibit a similar shape at different current densities, with a gradual decline in product capacity and a less pronounced charge-discharge plateau observed as the current density increases. Additionally, an increased polarization between the discharge-charge curves is observed with higher current densities. This could be attributed to inefficient utilization of some embedded ammonium positions during high current and rapid charge-discharge processes, leading to changes in the embedded ammonium behavior of the material.

In order to explicate the electrochemical kinetics of ammonium vanadate ion batteries, a series of cyclic voltammetry (CV) tests were conducted on $NH_4V_4O_{10}$, $(NH_4)_2V_3O_8$ and $(NH_4)_2V_6O_{16}$ electrodes. Figure 4 illustrates the CV curves for the $NH_4V_4O_{10}$ electrode with an escalation in scan rate from 0.2 mV s^{-1} to 1.0 mV s^{-1} using a 0.5 mol $L^{-1}(NH_4)_2SO_4$ electrolyte. In particular, in Fig. 4a, the CV curves evince two pairs of reduction/oxidation peaks proximate to -0.47/0.09 V and − 0.24/1.07 V, respectively. This implies that there is a multistep reversible NH_4^+ insertion/deinsertion process[29], which can also be delineated by its charge/discharge curves. It is widely acknowledged that the rate of NH_4^+ insertion/deinsertion in layered compounds is heavily influenced by intrinsic properties, notably the diffusion behavior of NH_4^+ within the compound. Mathematical formulations (Equations 1 and 2) elucidate the relationship between current (i) and scan rate (v), thereby facilitating a qualitative analysis of capacitive effects[30]: $i = avb$ (1); $\log(i) = b\log(v) + \log a$ (2). Peak current b values are utilized to classify charge storage mechanisms as either battery-like (b = 0.5) or capacitor-like (b = 1.0), providing valuable insights into electrochemical performance. The computed b values for the peaks numbered 1 through 4 are 0.64, 0.87, 0.81, and 0.62, respectively (as depicted in Fig. 4b), signifying that the electrochemical kinetics is determined by a confluence of capacitance-controlled and diffusion-controlled behavior. The corresponding currents at varying scan rates can be represented by Eq. (3)[31]: $i(V) = k_1v + k_2v^{1/2}$ (3), where k_1v and $k_2v^{1/2}$ represent the capacitive and diffusion-controlled processes, correspondingly. Taking Fig. 4c (0.2 mV s^{-1}) as an

instance, the blue area denotes the capacitive contribution while the remaining region of the CV profile signifies the diffusion control contribution. As demonstrated in Fig. 4h, at a scan rate of 0.5 mol L^{-1} $(NH_4)_2SO_4$ electrolyte, the calculated capacitance contributions of $NH_4V_4O_{10}$ electrode were found to be 54%, 61%, 69%, 70%, and 74% for scan rates of 0.2, 0.4, 0.6, 0.8 and 1.0 mV s^{-1} severally. Remarkably, the response current is primarily derived from surface control capacitance during low-scan scans surpassing that of capacitance contribution from $(NH_4)_2V_3O_8$ and $(NH_4)_2V_6O_{16}$ electrodes at an identical scan rate within a range of concentrations of up to .0.5 mol L^{-1} $(NH_4)_2SO_4$ electrolyte. The role played by capacitive processes in electrochemical reaction gradually increases with an increase in scan rate over time.

In rudimentary electrochemistry, the mechanism of charge transfer within a cell encompasses intercalation, conversion, and deposition reactions[32, 33]. Within the intercalation process, redox reactions occur within the host material and are accompanied by phase transitions (as depicted in Fig. 4i(a)). Conversely, NH_4^+ storage in pseudo capacitor materials relies on Faraday redox reaction and exhibits electrical traits that resemble those of a capacitor. In practical application, most vanadium-based pseudocapacitive materials do not exhibit perfect box-shaped cyclic voltammograms (CVs) akin to those of capacitors. Pseudo capacitances can be classified into three primary categories[34]: (1) underpotential deposition, which refers to the electrodeposition of a metal monolayer onto a heterogeneous metal substrate at a substantially lower potential than deposition on the same metal surface with an adsorbate (not addressed herein); (2) surface or near-surface redox pseudo capacitance, whose properties are largely influenced by the surface characteristics of the nanostructured material (depicted in Fig. 4i(b)); and (3) intercalation pseudo capacitance, where charge storage occurs not at the surface but within the crystal structure of the material possessing 1D, 2D, or 3D channels (illustrated in Fig. 4i(c)). The principal advantage of intercalation pseudo capacitance lies in its ability to enable swift charging within a short period due to suppression of solid-state phase transition and negligible lattice strain[35].

The quantitative analysis of cyclic voltammetry test data indicates that the $NH_4V_4O_{10}$ electrode's capacitance contribution is higher under 0.5 mol L^{-1} $(NH_4)_2SO_4$ electrolyte compared to that under 0.5 mol L^{-1} K_2SO_4 electrolyte and 0.5 mol L^{-1} Na_2SO_4 electrolyte. Given the electrode's convenient two-dimensional ion channel diffusion pathway, outstanding fast charge and discharge properties, and small specific surface area, it is reasonable to deduce that the $NH_4V_4O_{10}$ material exhibits intercalation pseudo capacitance behavior instead of surface redox pseudo capacitance.

To gain a more profound comprehension of the complexities of the electrochemical behavior of ammonium vanadate, determining the NH_4^+ diffusion coefficient can provide additional illumination. The diffusion coefficients were obtained by means of constant-current intermittent titration (GITT), and the calculation was based on a secondary titration discharge/charge cycle. As illustrated in the diagram, $NH_4V_4O_{10}$ demonstrated the highest diffusion coefficient (ranging from 2.09×10^{-6} to 3.66×10^{-6} cm^2 s^{-1}) during the discharge process, due to its generous planar spacing which allowed for a greater number of

sites for the rapid migration of $NH_4V_4O_{10}$ during the electrochemical reaction. Furthermore, the relatively high diffusion coefficient of $(NH_4)_2V_3O_8$ (ranging from 2.50×10^{-8} to 1.63×10^{-6} cm^2 S^{-1}) can be attributed to its tunneling architecture, which potentially provides it with an effective NH_4^+diffusion pathway. The diffusion coefficient of $(NH_4)_2V_6O_{16}$ ranged from 6.15×10^{-8} to 1.72×10^{-6} cm^2 s^{-1}, which was accompanied by a decrease in its capacity upon decreasing cycling. It is worth noting that the calculated NH_4^+ diffusion coefficient in $NH_4V_4O_{10}$ during NH_4^+ detachment is significantly lower than that during insertion, due to the challenge of NH_4 + extraction, which may be responsible for its capacity decay.

In order to elucidate the structural evolution and chemical state changes of $NH_4V_4O_{10}$ during NH_4^+ insertion/extraction, XRD, FTIR, and XPS spectra were acquired for different charge states. The non-in situ XRD spectra for various charge/discharge states are depicted in Figs. 6a and 6b. The initial NH_4^+ insertion process results in the formation of a tetragonal crystalline phase, $(NH_4)_{1.92}V_3O_8$ (PDF#51-1733), as evidenced by the enlarged region of Fig. 6b. The shift of the (001) peak to a higher angle can be attributed to the generation of a new phase. During charging, the (001) peak shifts from 8.78° to 8.94° towards a higher 2θ value, indicating a decrease in the interlayer distance, which is likely caused by NH_4^+ deintercalation. The highly reversible structural evolution of $NH_4V_4O_{10}$ during charging and discharging is an inherent manifestation of its exceptional cycling performance.

During the initial discharge/charge cycle, in-situ Fourier Transform Infrared (FTIR) spectroscopy was employed, as depicted in the left panel of Fig. 6c. Throughout the first discharge, the interlayer region was gradually infiltrated by ammonium ions (NH_4^+), resulting in a slight red shift of the V = O peak, which indicated a reduction in V elements[36] and an increase in V = O—H hydrogen bonding. Subsequently, during the charging phase, NH_4^+ was extracted, causing a decrease in the V = O—H hydrogen bond peak. Conversely, during the discharge phase, the insertion of NH4 + led to an elevation in the V = O—H hydrogen bond peaks. As depicted in the right panel of Fig. 6c, the peak located at 3285 cm-1 corresponds to the stretching vibration of the N-H bond[37, 38]. Throughout the discharge process, its intensity progressively amplifies and undergoes a similar shift towards the lower wave numbers, implying the successful embedding of NH_4^+ and the formation of hydrogen bonds with the oxygen atoms of $NH_4V_4O_{10}$. During the charging process, NH_4^+ gradually disengages, whereas the hydrogen bonds are disrupted. Hence, it has been demonstrated that the embedding and de-embedding of NH_4^+ within the $NH_4V_4O_{10}$ electrode are accomplished through the formation and cleavage of hydrogen bonds.

Moreover, ex-situ X-ray photoelectron spectroscopy (XPS) analyses were conducted at various stages of the $NH_4V_4O_{10}$ charging and discharging process. As illustrated in Figs. 6d, the N 1s peak gradually increases during the discharge phase and subsequently decreases to its original state during charging. Additionally, the O 1s spectrum (Figs. 6e) indicates that the peak at 530.3 eV corresponds to the -VO- bond. Notably, a new signal emerges at 531.2 eV after discharge, which can be attributed to N–H–O

bonds. This finding suggests that NH_4^+ is incorporated into $NH_4V_4O_{10}$, forming N–H–O hydrogen bonds with the $NH_4V_4O_{10}$ layer[39]. After the charging process, the N–H–O peak in O 1s displays a decrease, indicating the deembedding of NH_4^+. However, a small fraction of NH_4^+ remains embedded. This phenomenon ultimately results in the disintegration of the $NH_4V_4O_{10}$ lattice structure due to expansion during long-term cycling, leading to a decline in capacity. The charging process (e ~ g) in the N 1s spectrum further supports this observation, where the peaks located at 399.7 eV and 401.5 eV correspond to -N-H-(NH_3) and -N + H-(NH_4^+), respectively[40, 41]. During the N 1s spectral discharge (g ~ j), the -N-H-/-N + H- ratio is significantly higher than the original state as more intercalated ammonium ions are present in the form of NH_3, which is consistent with prior research[42]. In contrast, during the first discharge (a ~ c), the embedded ammonium ions generate a new phase $(NH_4)_{1.92}V_3O_8$, leading to a significant decline in the -N-H-/-N + H- ratio compared to the pristine state (Figs. 6f).

The unique oriented hydrogen bonding chemistry of NH_4^+ with the host material clarifies why NH_4^+ and K^+ have similar radii and magnitudes of interaction, yet exhibit different pseudocapacitive storage behavior. While spherical K^+ and Na^+ lack a preferred orientation, NH_4^+ displays a tetrahedral shape that allows it to twist and rotate during migration within $NH_4V_4O_{10}$, maintaining coordination of hydrogen bonding with adjacent oxygen atoms. This exceptional mechanical structure may or may not be a ubiquitous phenomenon in various layered materials.

5. Conclusions

In summary, we have utilized a simple hydrothermal method to synthesize a variety of ammonium vanadates with unique planar spacing, which were subsequently utilized as cathodes in aqueous ammonium ion batteries. Through the investigation of the diverse local structures of ammonium vanadate, we have gained valuable insights into the fundamental mechanisms that underlie its exceptional electrochemical performance. Specifically, $NH_4V_4O_{10}$ features a robust bilayer architecture, in which the NH_4^+ cation located between the vanadium oxygen layers acts as a "pillar", imparting structural stability and mitigating volumetric variations during the intercalation/deintercalation of guest ions in the interlayer spacing or channels. The $NH_4V_4O_{10}$ material that has been prepared boasts the largest interplanar distance of 9.8 Å and the highest diffusion coefficient, resulting in exceptional electrochemical performance. At a current density of 0.5 A g^{-1}, it delivers a discharge specific capacity of 297 mAh g^{-1} and an impressive multiplicative performance of 97 mAh g^{-1}@10 A g^{-1}. When combined with polyaniline to form an aqueous ammonium ion full cell, it delivers a specific capacity of 88 mAh g-1 (0.5 A g^{-1}) and an energy density of 88 Wh kg^{-1} (energy density of 500 W kg^{-1}), making it a highly efficient and cost-effective option. The pseudocapacitive properties of $NH_4V_4O_{10}$ are primarily attributed to the reversible embedding/deembedding behavior of NH_4^+ within the $NH_4V_4O_{10}$ framework. The mechanism of NH_4^+ storage within $NH_4V_4O_{10}$ has been studied, revealing that during the first embedding of ammonium ions, $NH_4V_4O_{10}$ undergoes a phase transition and transforms into $(NH_4)_{1.92}V_3O_8$. The highly reversible

insertion/detachment process of NH_4^+ is always accompanied by the formation/breakage of hydrogen bonds during the interlayer tunneling of $NH_4V_4O_{10}$. As such, the $NH_4V_4O_{10}$ cathode is a highly promising and safe option for aqueous ammonium ion batteries, offering exceptional performance and cost-effectiveness.

Declarations

Ethical Approval

All analyses were based on previous published studies, thus no ethical approval and patient consent are required.

Competing interests

I declare that the authors have no competing interests as defined by Springer, or other interests that might be perceived to influence the results and/or discussion reported in this paper.

Authors' contributions

Junjun Wang: Writing- Original draft preparation.

Kaixiong Xiang: Writing- Reviewing and Editing.

Xiaoyu Wen Data analysis and experimentation.

Han Chen: Conceptualization, Methodology.

Jingxiong Liu: Supervision, Validation.

All authors reviewed the manuscript.

Funding

This work is supported by the National Natural Science Foundation of China (52171200, 52371211) and Changsha Special Project (kh2301006), Excellent youth funding of Hunan Provincial Education Department (22B0588), Key research and development project of Hunan Province (2022GK2049), National Sustainable Development Innovation Demonstration Zone project(2022sfq09).

Availability of data and materials

The authors confirm that the data supporting the findings of this study are available within the article [and/or its supplementary materials].

References

1. Wei J, Zhang P, Liu Y, Zhu M, Dai T, Tie Z, et al. Wide-voltage-window amphiphilic supramolecule excluded-volume electrolytes for ultra-durable full-cell aqueous potassium-Ion batteries. Chemical Engineering Journal 2023; 459:141623.
2. Sarkar A, Sarkar S, Sarkar T, Kumar P, Bharadwaj MD, Mitra S. Rechargeable sodium-ion battery: high-capacity ammonium vanadate cathode with enhanced stability at high rate. ACS Applied Materials & Interfaces 2015; 7(31):17044–17053.
3. Song TB, Huang ZH, Zhang XR, Ni JW, Xiong HM. Nitrogen-Doped and Sulfonated Carbon Dots as a Multifunctional Additive to Realize Highly Reversible Aqueous Zinc-Ion Batteries. Small 2023:2205558.
4. Zhang S, Wang Y, Sun Y, Wang Y, Yang Y, Zhang P, et al. High-Energy Aqueous Magnesium Ion Batteries with Capacity-Compensation Evolved from Dynamic Copper Ion Redox. Small 2023:2300148.
5. Qin Z, Song Y, Liu Y, Liu X-X. Aqueous calcium-ion storage in amorphous molybdenum oxide. Chemical Engineering Journal 2023; 451:138681.
6. Ran Q, Zeng SP, Zhu MH, Wan WB, Meng H, Shi H, et al. Uniformly MXene-Grafted Eutectic Aluminum-Cerium Alloys as Flexible and Reversible Anode Materials for Rechargeable Aluminum-Ion Battery. Advanced Functional Materials 2023; 33(1):2211271.
7. Wu X, Qi Y, Hong JJ, Li Z, Hernandez AS, Ji X. Rocking-chair ammonium-ion battery: a highly reversible aqueous energy storage system. Angewandte Chemie International Edition 2017; 56(42):13026–13030.
8. Su Z, Chen J, Stansby J, Jia C, Zhao T, Tang J, et al. Hydrogen-Bond Disrupting Electrolytes for Fast and Stable Proton Batteries. Small 2022; 18(22):2201449.
9. Su Z, Tang J, Chen J, Guo H, Wu S, Yin S, et al. Co-insertion of Water with Protons into Organic Electrodes Enables High-Rate and High-Capacity Proton Batteries. Small Structures 2023; 4(3):2200257.
10. Wessells CD, Peddada SV, McDowell MT, Huggins RA, Cui Y. The effect of insertion species on nanostructured open framework hexacyanoferrate battery electrodes. Journal of The Electrochemical Society 2011; 159(2):A98.
11. Dong S, Shin W, Jiang H, Wu X, Li Z, Holoubek J, et al. Ultra-fast NH4 + storage: strong H bonding between NH4 + and bi-layered V2O5. Chem 2019; 5(6):1537–1551.
12. Xu L, Zhang Y, Jiang H, Zheng J, Dong X, Hu T, et al. Facile hydrothermal synthesis and electrochemical properties of (NH4) 2V6O16 nanobelts for aqueous rechargeable zinc ion batteries. Colloids and Surfaces A: Physicochemical and Engineering Aspects 2020; 593:124621.
13. Zong Q, Wang Q, Liu C, Tao D, Wang J, Zhang J, et al. Potassium ammonium vanadate with rich oxygen vacancies for fast and highly stable Zn-ion storage. ACS nano 2022; 16(3):4588–4598.
14. Li H-Y, Wang L, Wei C, Li X, Xie B. Synthesis of ultralong (NH4) 2V6O16· 1.5 H2O nanobelts for application in supercapacitors. Materials Technology 2015; 30(sup2):A109-A114.

15. Wang H, Huang K, Huang C, Liu S, Ren Y, Huang X. (NH4) 0.5 V2O5 nanobelt with good cycling stability as cathode material for Li-ion battery. Journal of Power Sources 2011; 196(13):5645–5650.
16. He H, Shang Z, Huang X, Tan S, Sun D, Xu G, et al. Ultrathin (NH4) 0.5 V2O5 nanosheets as a stable anode for aqueous lithium ion battery. Journal of the Electrochemical Society 2016; 163(10):A2349.
17. Ottmann A, Zakharova G, Ehrstein B, Klingeler R. Electrochemical performance of single crystal belt-like NH4V3O8 as cathode material for lithium-ion batteries. Electrochimica Acta 2015; 174:682–687.
18. Lee J, Urban A, Li X, Su D, Hautier G, Ceder G. Unlocking the potential of cation-disordered oxides for rechargeable lithium batteries. *science* 2014; 343(6170):519–522.
19. He T, Ye Y, Li H, Weng S, Zhang Q, Li M, et al. Oxygen-deficient ammonium vanadate for flexible aqueous zinc batteries with high energy density and rate capability at – 30 C. Materials Today 2021; 43:53–61.
20. Zhao M, Zheng Q, He X, Ahmed I, Su Z, Tangsee S, et al. Enhanced Rate Capability and Cycling Stability of Novel Ammonium Vanadate Materials Used in Aqueous Li-Ion Batteries. 2021.
21. Zakharova G, Ottmann A, Ehrstein B, Klingeler R. Microwave-assisted hydrothermal synthesis of NH4V3O8 microcrystals with controllable morphology. Materials Research Bulletin 2016; 83:225–229.
22. Xu G, He H, Wan H, Liu R, Zeng X, Sun D, et al. Facile synthesis and lithium storage performance of (NH 4) 2 V 3 O 8 nanoflakes. Journal of Applied Electrochemistry 2016; 46:879–885.
23. Xu Y, Han X, Zheng L, Yan W, Xie Y. Pillar effect on cyclability enhancement for aqueous lithium ion batteries: a new material of β-vanadium bronze M 0.33 V 2 O 5 (M = Ag, Na) nanowires. Journal of Materials Chemistry 2011; 21(38):14466–14472.
24. Meng J, Liu Z, Niu C, Xu X, Liu X, Zhang G, et al. A synergistic effect between layer surface configurations and K ions of potassium vanadate nanowires for enhanced energy storage performance. Journal of Materials Chemistry A 2016; 4(13):4893–4899.
25. Zong Q, Du W, Liu C, Yang H, Zhang Q, Zhou Z, et al. Enhanced reversible zinc ion intercalation in deficient ammonium vanadate for high-performance aqueous zinc-ion battery. Nano-Micro Letters 2021; 13(1):116.
26. Wang Q, Zhang Y, Jiang H, Meng C. In-situ grown manganese silicate from biomass-derived heteroatom-doped porous carbon for supercapacitors with high performance. Journal of colloid and interface science 2019; 534:142–155.
27. Zheng J, Liu C, Tian M, Jia X, Jahrman EP, Seidler GT, et al. Fast and reversible zinc ion intercalation in Al-ion modified hydrated vanadate. Nano Energy 2020; 70:104519.
28. Bin D, Liu Y, Yang B, Huang J, Dong X, Zhang X, et al. Engineering a high-energy-density and long lifespan aqueous zinc battery via ammonium vanadium bronze. ACS applied materials & interfaces 2019; 11(23):20796–20803.
29. Wei T, Li Q, Yang G, Wang C. Highly reversible and long-life cycling aqueous zinc-ion battery based on ultrathin (NH) V O · 8H O nanobelts. 2018.

30. Lindström H, Södergren S, Solbrand A, Rensmo H, Hjelm J, Hagfeldt A, et al. Li + ion insertion in TiO2 (anatase). 2. Voltammetry on nanoporous films. The Journal of Physical Chemistry B 1997; 101(39):7717–7722.
31. Wang J, Polleux J, Lim J, Dunn B. Pseudocapacitive contributions to electrochemical energy storage in TiO2 (anatase) nanoparticles. The Journal of Physical Chemistry C 2007; 111(40):14925–14931.
32. Li F, Zhou Z. Micro/nanostructured materials for sodium ion batteries and capacitors. Small 2018; 14(6):1702961.
33. Delmas C. Sodium and sodium-ion batteries: 50 years of research. Advanced Energy Materials 2018; 8(17):1703137.
34. Augustyn V, Simon P, Dunn B. Pseudocapacitive oxide materials for high-rate electrochemical energy storage. Energy & Environmental Science 2014; 7(5):1597–1614.
35. Chao D, Fan HJ. Intercalation pseudocapacitive behavior powers aqueous batteries. Chem 2019; 5(6):1359–1361.
36. Han C, Zhu J, Fu K, Deng D, Luo W, Mai L. A high-capacity polyaniline-intercalated layered vanadium oxide for aqueous ammonium-ion batteries. Chemical Communications 2022; 58(6):791–794.
37. Majumdar A, Scholz G, Hippler R. Structural characterization of amorphous hydrogenated-carbon nitride (aH-CNx) film deposited by CH4/N2 dielectric barrier discharge plasma: 13C, 1H solid state NMR, FTIR and elemental analysis. Surface and Coatings Technology 2009; 203(14):2013–2016.
38. Zecchina A, Marchese L, Bordiga S, Paze C, Gianotti E. Vibrational spectroscopy of NH4 + ions in zeolitic materials: An IR study. The Journal of Physical Chemistry B 1997; 101(48):10128–10135.
39. Yu D, Wei Z, Zhang X, Zeng Y, Wang C, Chen G, et al. Boosting Zn2 + and NH4 + Storage in Aqueous Media via In-Situ Electrochemical Induced VS2/VOx Heterostructures. Advanced Functional Materials 2021; 31(11):2008743.
40. Sarkar T, Kumar P, Bharadwaj MD, Waghmare U. Structural transformation during Li/Na insertion and theoretical cyclic voltammetry of the δ-NH 4 V 4 O 10 electrode: a first-principles study. Physical Chemistry Chemical Physics 2016; 18(14):9344–9348.
41. Shi X-H, Chen L, Liu B-W, Long J-W, Xu Y-J, Wang Y-Z. Carbon fibers decorated by polyelectrolyte complexes toward their epoxy resin composites with high fire safety. Chinese Journal of Polymer Science 2018; 36:1375–1384.
42. Meng X, Wang H-N, Wang X-K, Dong L-Z, Zou Y-H. Cations mediating proton conductivity in an oxalate based microporous coordination polymer. New Journal of Chemistry 2019; 43(1):24–27.

Figures

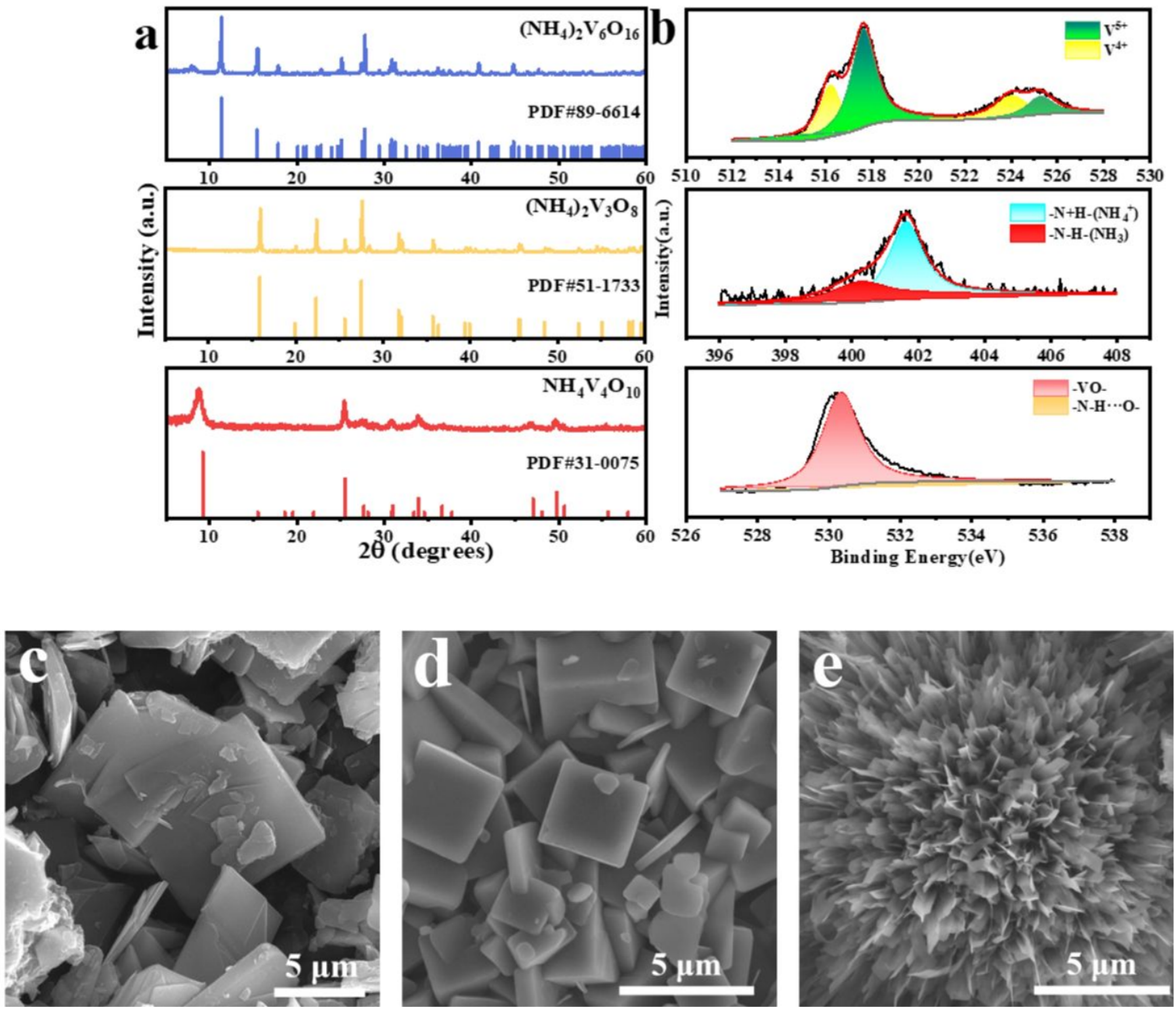

Figure 1

(a) XRD patterns of $(NH_4)_2V_6O_{16}$, $(NH_4)_2V_3O_8$ and $NH_4V_4O_{10}$; (b) high-resolution spectra of V 2p, N 1s and O 1s corresponding for $NH_4V_4O_{10}$. (c-e) SEM images of $(NH_4)_2V_6O_{16}$, $(NH_4)_2V_3O_8$ and $NH_4V_4O_{10}$

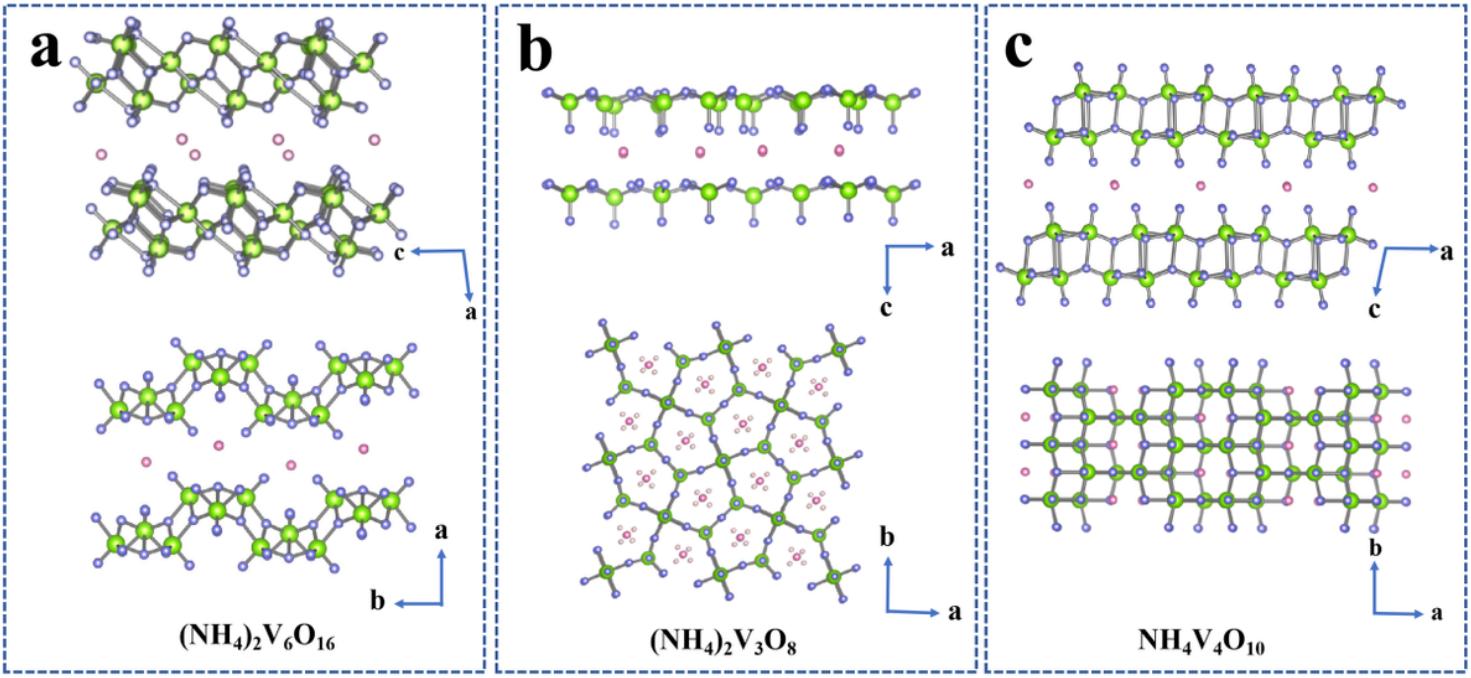

Figure 2

(a-c) $(NH_4)_2V_6O_{16}$, $(NH_4)_2V_3O_8$ and $NH_4V_4O_{10}$ atomic structures, the blue balls represent O atoms, the green and pink balls represent V atoms and NH_4^+

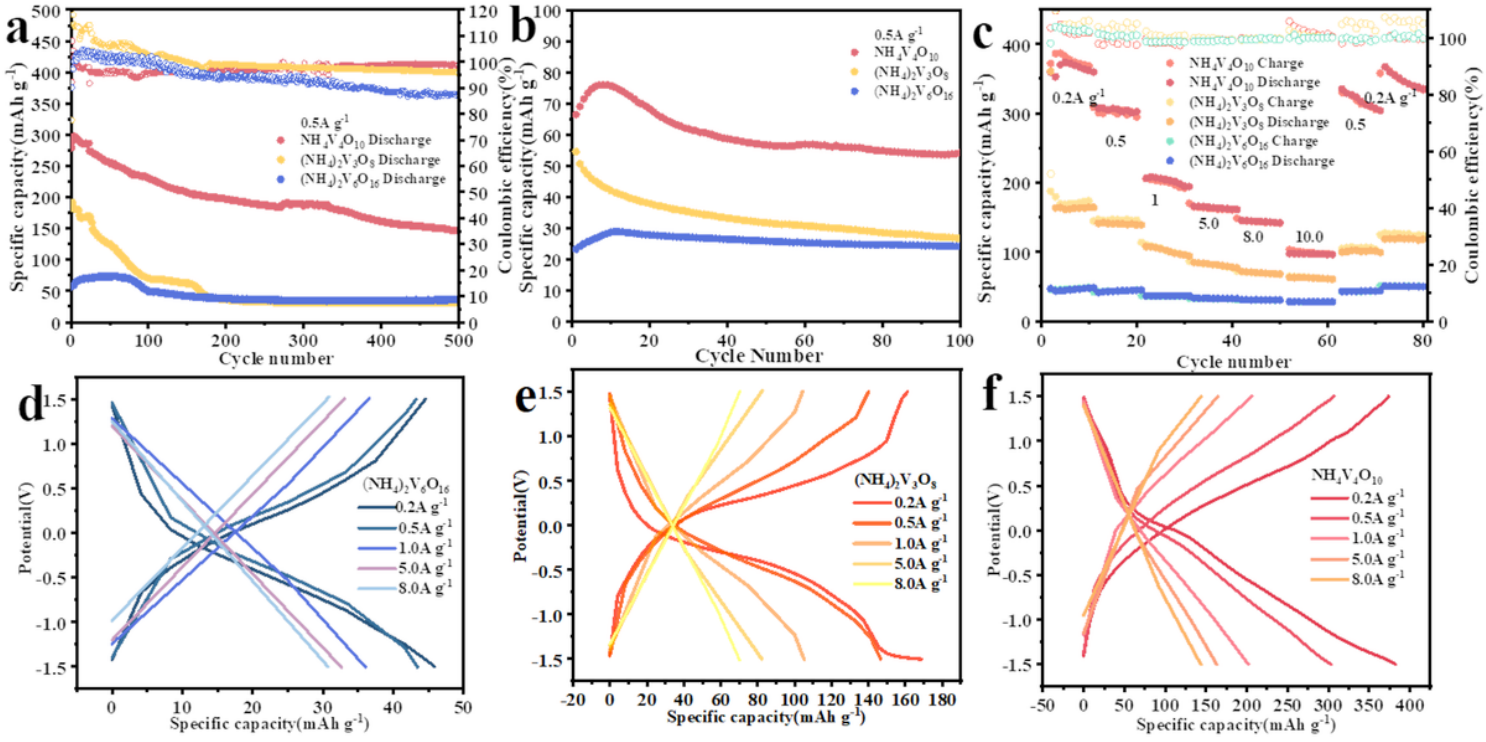

Figure 3

(a) 300 cycle diagram of $(NH_4)_2V_6O_{16}$, $(NH_4)_2V_3O_8$ and $NH_4V_4O_{10}$ electrodes at 0.5A g^{-1} current density in 0.5 mol L^{-1} $(NH_4)_2SO_4$ electrolyte; (b) 100 cycle diagram of $(NH_4)_2V_6O_{16}$, $(NH_4)_2V_3O_8$ and $NH_4V_4O_{10}$ electrodes and CC@PANI assembled into A button cell at 0.5 A g^{-1} current density; (c) Rate performance diagrams of different current densities in 0.5 mol L^{-1} $(NH_4)_2SO_4$ electrolyte; (d-f) Charge/discharge curves of $(NH_4)_2V_6O_{16}$, $(NH_4)_2V_3O_8$ and $NH_4V_4O_{10}$ electrodes at different current densities in 0.5 mol L^{-1} $(NH_4)_2SO_4$ electrolyte

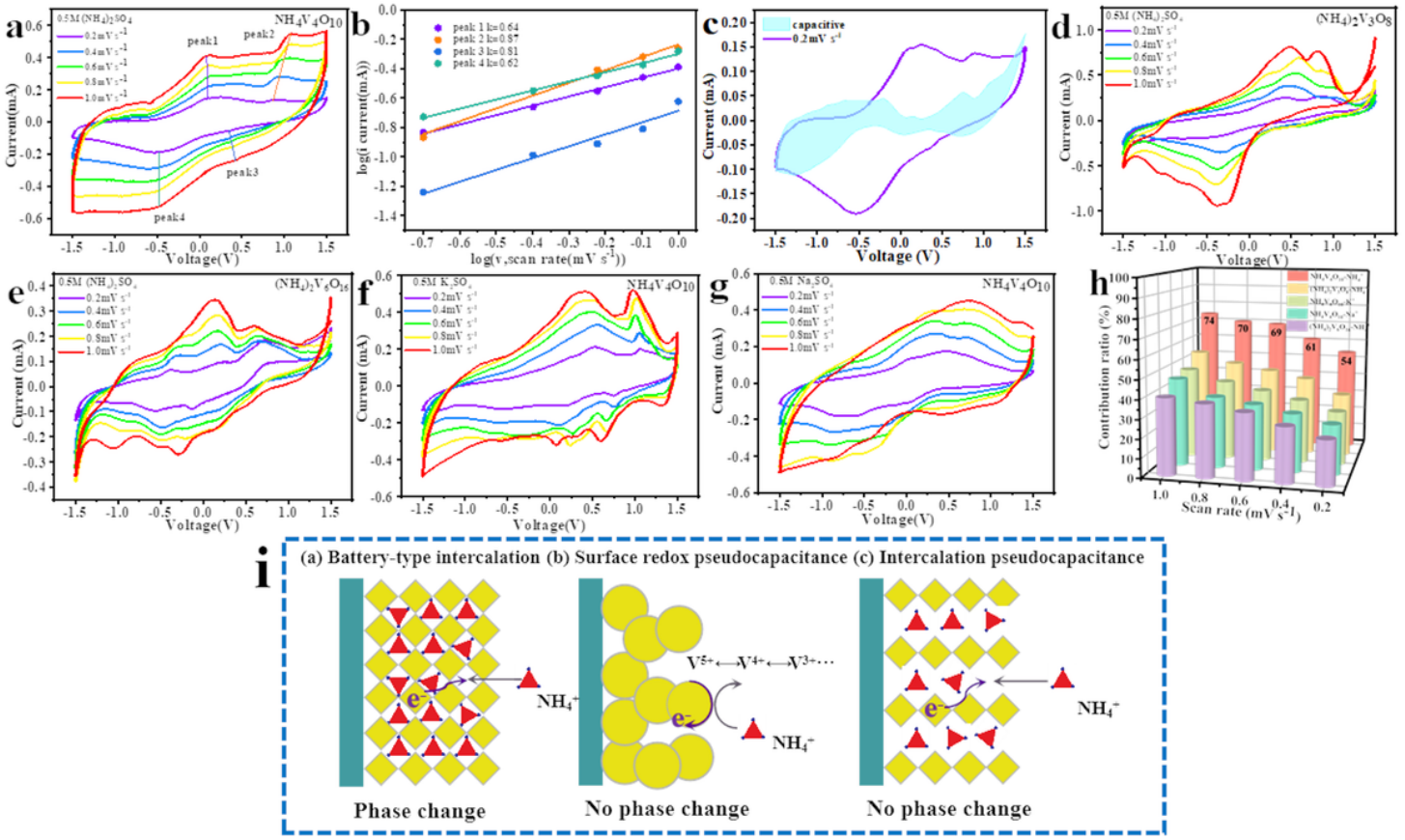

Figure 4

(a) CV curves of $NH_4V_4O_{10}$ at different scan rates under 0.5 mol L^{-1} $(NH_4)_2SO_4$ electrolyte; (b) log (i) vs. log (v) plots for specific peak currents in the CV curves in Figure 4 a; (c) capacity separation curves at 0.2 mV s^{-1}; (d) CV curves of $(NH_4)_2V_3O_8$ at 0.5 mol L^{-1} $(NH_4)_2SO_4$ electrolyte at different scan rates; (e) CV curves of $(NH_4)_2V_6O_{16}$ at 0.5 mol L^{-1} $(NH_4)_2SO_4$ electrolyte at different scan rates; (f) CV curves of $NH_4V_4O_{10}$ at 0.5 mol L^{-1} K_2SO_4 electrolyte at different scan rates; (g) CV curves of $NH_4V_4O_{10}$ at different scan rates under 0.5 mol L^{-1} Na_2SO_4 electrolyte; (h) histograms showing the percentage contribution of pseudo capacitance for each sample at different scan rates with different electrolytes; (i) from left to right, schematic diagrams of cell-type intercalation, surface redox pseudo capacitance, and intercalation pseudo capacitance, respectively

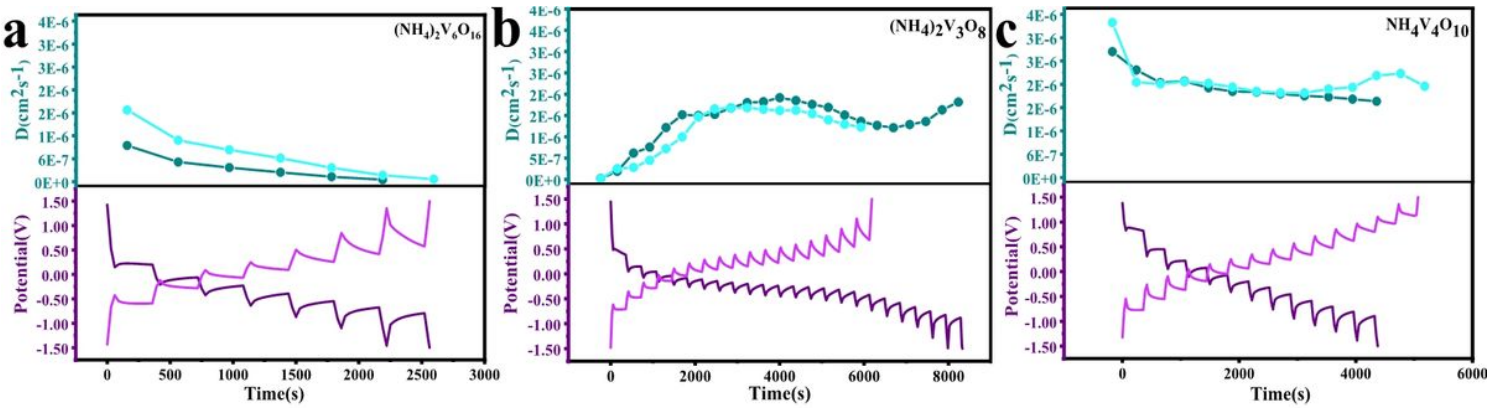

Figure 5

(a-c) GITT curves of $(NH_4)_2V_6O_{16}$, $(NH_4)_2V_3O_8$ and $NH_4V_4O_{10}$ and the corresponding NH_4^+ diffusion coefficients

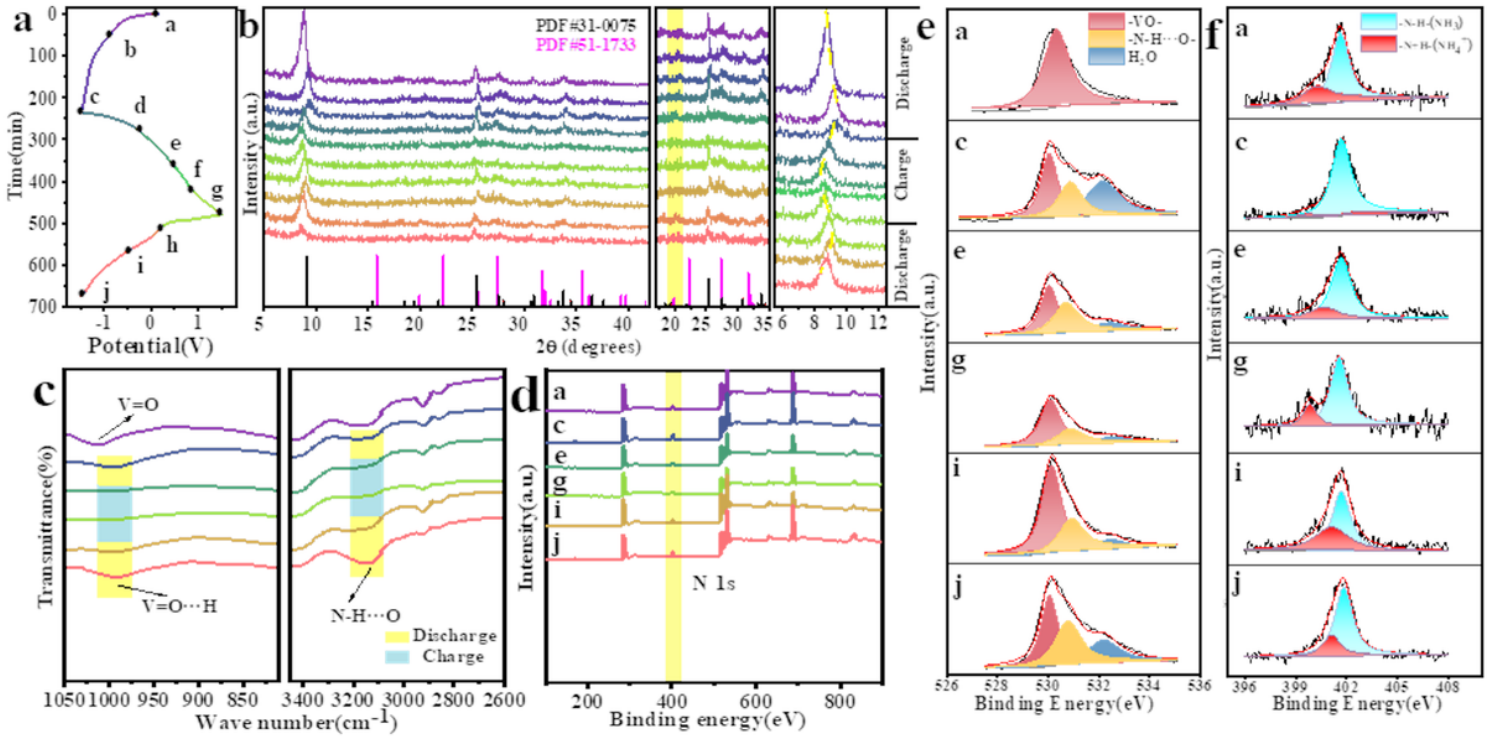

Figure 6

(a) First charge/discharge curves of $NH_4V_4O_{10}$ electrode; (b) corresponding ex situ XRD patterns at selected potentials; (c) FT-IR spectra, (d) XPS spectra and (e-f) high-resolution spectra of O 1s and N 1s corresponding to $NH_4V_4O_{10}$ at different potentials